Jpn. J. Appl. Phys. Vol. 39 (2000) pp. 6062–6066
Part 1, No. 10, October 2000

Characterization of an Imaging Extreme-Ultraviolet Flat-Field Spectrometer and Its Application to Extreme-Ultraviolet Emission Profile Measurement

Jaehoon KIM and Dong-Eon KIM

Department of Physics, Pohang University of Science and Technology, San 31 Hyojadong, Pohang, Kyungbuk 790-784, Republic of Korea

(Received January 19, 2000; accepted for publication June 15, 2000)

The spatial imaging property of an extreme-ultraviolet (XUV) flat-field spectrometer was studied using ray-tracing and measured experimentally. Under the condition that the spectrometer is stigmatic at 10 nm, ray-tracing simulations show that the spatial resolution is expected to be about 18 μm in the wavelength range from 2.5 nm to 30 nm. The measurement of the spatial resolution, using a wire as fiducial 20 mm away from the source position along the optical axis, was carried out for the CV resonance line (4.03 nm) and a spatial resolution of 70 μm was obtained. This value agrees well with the ray-tracing result for a source displaced 20 mm along the optical axis. Using the spatial imaging property of this spectrometer, the emission profiles of CV $1s^2$–$1s3p$ (3.50 nm) and CVI L_β (2.85 nm) lines from a laser-produced carbon plasma were measured. The spatial imaging property and Abel inversion were applied to laser-produced carbon plasma spectra to deduce emission profiles.

KEYWORDS: XUV spectrometer, Abel inversion, Laser-produced plasma, Imaging spectrometer, Emission profile, Toroidal mirror

1. Introduction

A spatially-resolving extreme-ultraviolet (XUV) spectrometer has been widely used in various plasma research such as laser plasma interaction,[1] soft X-ray laser study,[2] and absorption spectroscopy.[3] In this wavelength region, a grating must be set at a grazing incidence for high reflectivity.[4] However, grazing incidence spectrometers suffer from astigmatism and lack high-quality imaging ability. To obtain a spatial imaging capability, focusing optics such as a toroidal mirror have been placed in front of a grating.[5,6] The imaging property of a Rowland-circle spectrometer equipped with both a concave grating and a toroidal mirror was well studied.[6]

Another type of XUV spectrometer that has been widely used is a flat-field spectrometer equipped with a variable line-spacing concave grating.[7–12] In this spectrometer, the focal plane is flat so that flat detectors such as a photodiode array, an X-ray streak camera, and a microchannel plate (MCP) can be used easily. These flat-field spectrometers do not have spatial imaging capability. Focusing optics such as a toroidal mirror[11] and a combination of spherical and cylindrical mirrors[12] are also needed in these spectrometers for spatial imaging. The imaging property of a flat-field spectrometer with a toroidal mirror is different from a Rowland-circle spectrometer and was studied using the aberration theory.[11]

If a spectrometer has a spatial resolution, spectroscopic data from the spectrometer are line-integrated along the line of sight. If a source has a cylindrical symmetry, as in laser-produced plasma and Z-pinch plasma, the local emission profile can be deduced via Abel inversion.[13–15]

In this work, a spatially-resolving flat-field spectrometer with a toroidal mirror was constructed. The imaging property was studied using a ray-tracing code and measured using laser-produced carbon plasmas. Abel inversion was applied to deduce the emission profile as a function of radial distance from the symmetric axis.

2. Imaging Property of an XUV Flat-Field Spectrometer

2.1 Simulation using a ray-tracing code

The schematic optical layout of a flat-field spectrometer equipped with a toroidal mirror is shown in Fig. 1. The toroidal mirror focuses light from a source with different foci determined by the incidence angle in the horizontal and vertical plane. The toroidal mirror is set up so that the focusing property functions on a horizontal plane to collect light into the slit of the spectrometer and on a vertical plane to reduce astigmatism.[5,6,11] To satisfy these requirements, the optical parameters of the toroidal mirror are to be determined as follows.

First, in order for the toroidal mirror to focus light to the entrance slit of the spectrometer on a horizontal plane, the toroidal mirror must satisfy:

$$\frac{1}{r_{\mathrm{st}}} + \frac{1}{r_{\mathrm{ts}}} = \frac{2}{\rho_{\mathrm{h}} \cos\phi}, \tag{2.1}$$

where r_{st} is the distance from the source to the toroidal mirror, r_{ts} from the toroidal mirror to the entrance slit, ρ_{h} the major radius of the toroidal mirror, and ϕ the incidence angle to the

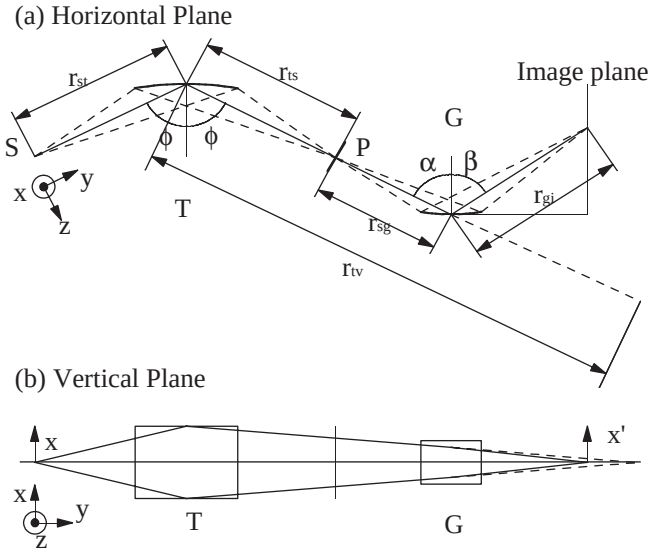

Fig. 1. Schematic diagram of the optical layout of an XUV flat-field spectrometer with a toroidal mirror (a) on a horizontal plane and (b) on a vertical plane. [S, source; T, toroidal mirror; P, entrance slit of the spectrometer; G, variable line-spacing concave grating; r_{st}, distance from source to toroidal mirror; r_{ts}, distance from toroidal mirror to entrance slit; r_{sg}, distance from entrance slit to grating; r_{tv}, distance from slit to vertical image due to toroidal mirror only; r_{gi}, distance from grating to image.]

toroidal mirror.

The toroidal mirror focuses the source vertically on an image plane, reducing astigmatism, according to the following equation:

$$\frac{1}{r_{st}} + \frac{1}{r_{tv}} = \frac{2\cos\phi}{\rho_v}, \tag{2.2}$$

where r_{tv} is the distance from the toroidal mirror to the image without the grating, and ρ_v the minor radius of the toroidal mirror. A virtual source for the grating is located at a distance of $r_{ts}+r_{sg}-r_{tv}$ and the concave grating focuses light according to:

$$\frac{1}{r_0} + \frac{1}{r_{gv}} = \frac{\cos\alpha + \cos\beta}{R}, \tag{2.3}$$

where r_0 is the distance from the grating to the virtual source ($= r_{ts} + r_{sg} - r_{tv}$), r_{gv} the distance from the grating to the vertical focal position, R the radius of curvature of the grating, α the incidence angle to the grating, and β the diffraction angle.

To obtain a stigmatic image, both eqs. (2.2) and (2.3) must be satisfied simultaneously; however, because of the wavelength dependence of the diffraction angle β in eq. (2.3), a stigmatic image is possible only for one wavelength. When the stigmatic wavelength is selected (in this work, we have chosen 10 nm.), r_0 is calculated using eq. (2.3). From this r_0 and fixed minor radius ρ_v, the incidence angle to the toroidal mirror has been chosen to satisfy eq. (2.2). The major radius of the toroidal mirror has been chosen using eq. (2.1).

The optical parameters of the spectrometer are summarized in Table I. With these parameters, the real image of a source is formed horizontally on the entrance slit of the spectrometer with a magnification of unity ($r_{st}/r_{ts} = 1$). The reversed real image of a source with a magnification of about 1.95 [$\sim (r_{tv}/r_{st}) \times (r_{gv}/r_0)$] for the 10 nm wavelength is formed vertically on an image plane.

To characterize the imaging property of this spectrometer, a ray-tracing code, SHADOW,[16] is used. In this simulation, a point source is used. The source divergence is selected to fit the entire toroidal mirror surface.

Ray-tracing results for this spectrometer are shown in Fig. 2. Figure 2(a) shows the images of several wavelengths on the image plane. Corresponding intensity profiles along the x' direction in Fig. 2(a) are shown in Fig. 2(b). The images do not change appreciably with the wavelength because the distances from a grating to the images do not vary in the case of a flat-field spectrometer as much as in the case of a Rowland-circle spectrometer.[6] The average of the full-width at half maximums (FWHMs) of the image profiles is about $35 \pm 5\,\mu$m in the wavelength range of 2.5 nm to 30 nm. The spatial resolution in a vertical direction defined by the FWHMs of the intensity profile is about $18\,\mu$m due to the vertical magnification for this spectrometer.

Table I. Optical parameters of the spectrometer.

Spectrograph	
Radius of curvature of the grating	$R = 5649$ mm
Nominal groove spacing	$\sigma_0 = 1200$ lines/mm
Angle of incidence to the grating	$\alpha = 87°$
Sagittally focused wavelength	$\lambda_0 = 10$ nm
Entrance slit width	$100\,\mu$m
Distance between slit and grating	$r_{sg} = 237$ mm
Tangential distance from grating to the image plane	$L = 235$ mm
Toroidal mirror	
Angle of incidence	$\phi = 86.078°$
Major radius	$\rho_h = 7310$ mm
Minor radius	$\rho_v = 45.25$ mm
Source to mirror	$r_{st} = 500$ mm
Mirror to entrance slit	$r_{ts} = 500$ mm
Mirror to image plane	$r_{tv} = 977.4$ mm
Size of mirror	200 mm × 15 mm

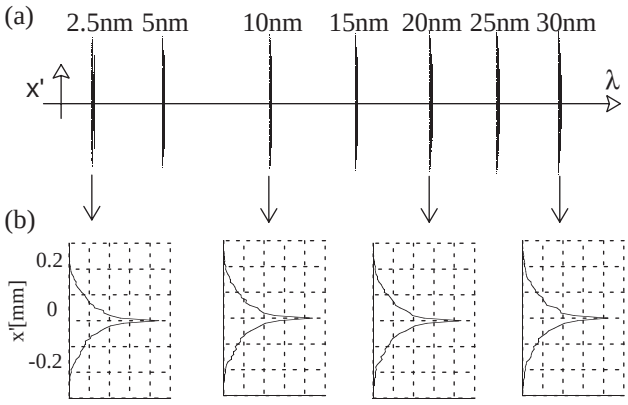

Fig. 2. (a) Ray-traced spot diagram of spectral lines on the image plane from a source on the optical axis. (b) Ray-traced intensity distribution is scanned along the direction perpendicular to the dispersion direction for several wavelengths.

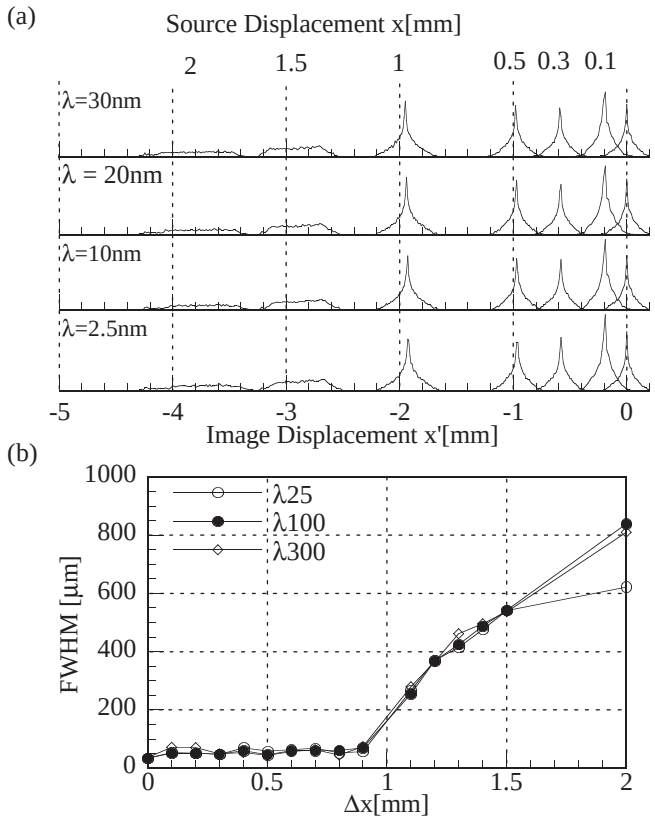

Fig. 3. (a) Intensity distribution changes of spectral lines on the image plane when the source is displaced along the x direction [Fig. 1(b)]. Ray-traced intensity distribution is scanned along the direction perpendicular to the dispersion direction for several wavelengths. (b) FWHMs of the image on the image plane for several wavelengths according to the source position along the x direction.

The effect of the source displacement along the x direction [in Fig. 1(b)] is shown in Fig. 3. Figure 3(a) shows the intensity profiles along the x' direction for several wavelengths when the source is displaced along the x direction. Until the source is displaced by about 1 mm, the intensity profiles do not vary significantly. Figure 3(b) shows the change of the FWHMs of the intensity distributions for several wavelengths with respect to the displacement. For the source displaced up to 1 mm, the FWHM is about 35 μm, implying that this system has a spatial resolution of about 18 μm along the x direction [in Fig. 1(b)] when the source is in the ± 1 mm range in the x direction from the optical axis.

Figure 4 shows the effect of the source displacement along the y direction [Fig. 1(b)]. The intensity profile of 10 nm light is shown in Fig. 4(a). Figure 4(b) shows FWHMs for several wavelengths. When the source is displaced along the y direction less than 15 mm, the FWHM is about 35 μm. This spectrometer can image the source with a spatial resolution of 18 μm when the source is within a ± 15 mm range along the y direction.

Figure 5 shows the effect of the source displacement along the z direction. Due to the entrance slit of the spectrometer used in the simulation and experiment, the width of the imaging region along the z axis in the source position is limited up to about 100 μm. This is why the intensity drops markedly beyond $\Delta z = \pm 50\,\mu$m.

These results indicate that a source displaced by about ± 1 mm along the x direction, ± 15 mm along the y direction, and $\pm 50\,\mu$m along the z direction in the source position can be imaged with a spatial resolution of about 18 μm.

2.2 *Experimental measurement of the spatial resolution of an imaging XUV flat-field spectrometer*

The spatial resolution of an imaging XUV flat-field spectrometer was measured using laser-produced carbon plasmas.

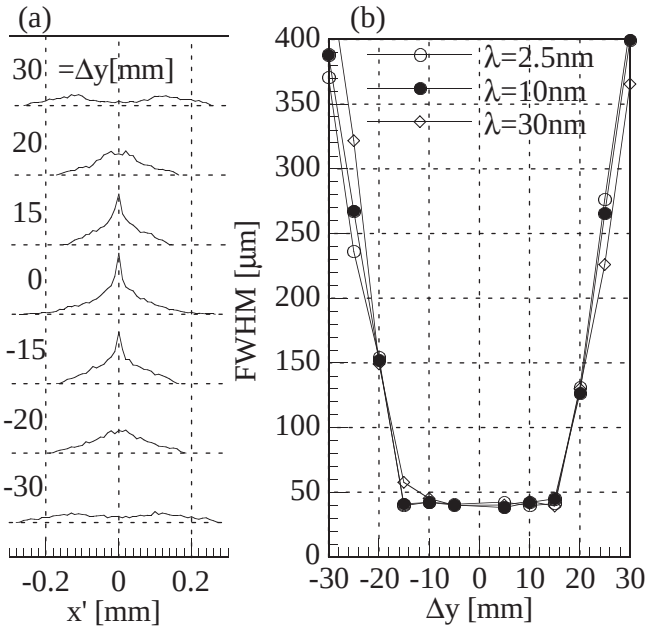

Fig. 4. (a) Intensity distribution on the image plane when a source is displaced along the y direction for 10 nm wavelength light. (b) FWHMs of the image when the source is displaced along the y direction for several wavelengths.

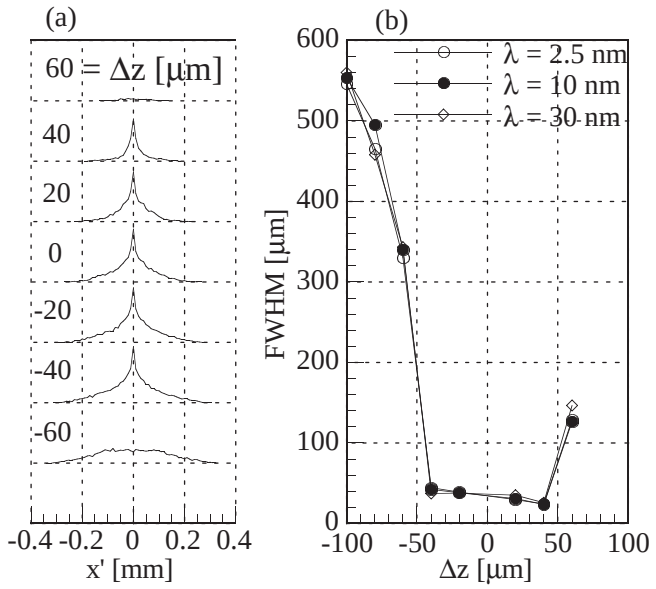

Fig. 5. (a) Intensity distribution on the image plane when a source is displaced along the z direction for 10 nm wavelength light. (b) FWHMs of the image when the source is displaced along the z direction for several wavelengths.

A Q-switched Nd/Glass laser with a pulse duration of 3 ns and an energy of 1 J was focused on a carbon target. Radiation from the plasmas is dispersed by the flat-field spectrometer on the image plane, on which a MCP is placed. The MCP is gated with an electric pulse of 10 ns FWHM from a gating circuit and thus time-resolved experiments with a time window of less than 10 ns are possible due to the dependence of the MCP gain upon the applied voltage.[17)]

A delay generator is used to synchronize the laser and the gating time. The delay generator triggers the laser Q-switch, and then the fast gating switch after a delay. The laser pulse is monitored in front of a target chamber and is compared with the gating pulse to determine the time difference between plasma generation and measurement time.

To measure the spatial resolution of the spectrometer, wires of approximately 720 μm in diameter were used as fiducials. They were placed 20 mm away from the source toward the

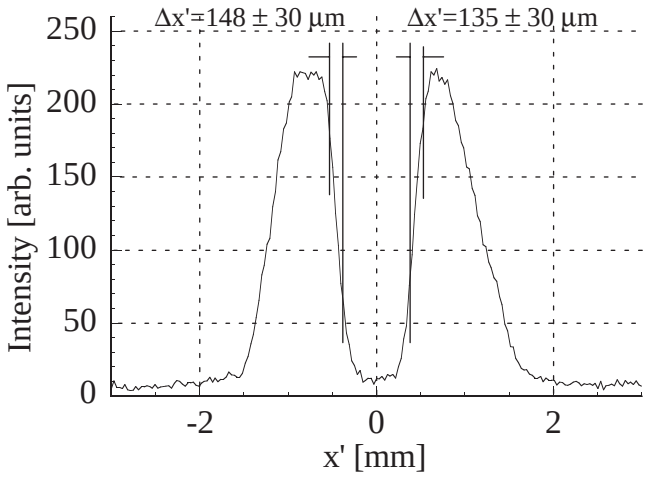

Fig. 6. Measured intensity distribution of the CV resonance line along the x'-direction on image plane in Fig. 1. $\Delta x'$ is the width over which the intensity ranges from 75% to 25%.

spectrometer along the optical axis. In this experiment, the gating was not used. The spectrum was obtained 600 μm away normal to the target surface [z direction in Fig. 1(a)]. Figure 6 is the intensity distribution of the CV resonance line along the x' direction (perpendicular to the dispersion direction). This intensity modulation represents the spatial imaging property when a source is displaced 20 mm along the y direction to the toroidal mirror. The spatial resolution, defined by the intensity change from 75% to 25%,[18] is about 140 μm on the image plane which corresponds to 72 μm on the source plane considering the vertical magnification. This value agrees well with the simulation results in Fig. 4(b): the intensity profile width in simulation is 130 μm with a source being displaced 20 mm along the y direction.

3. Emission Profile Measurement

3.1 Abel inversion

For a cylindrically symmetric, optically thin, extended radiation source, the measured value $I(x, \lambda)$ is the line integration along the line of sight.[13,14] If a local emission coefficient is $\epsilon(r, \lambda)$, the intensity $I(x, \lambda)$ outside this source is described as

$$I(x, \lambda) = \int_{\text{chord}} \epsilon(r, \lambda) dy = 2 \int_r^R \frac{\epsilon(r, \lambda)}{\sqrt{r^2 - x^2}} r \, dr, \quad (3.1)$$

for a particular wavelength λ, where x is a measurement point from the optical axis in the image plane, r the radial distance from the symmetric axis, and R the source size. The inversion from the measured $I(x, \lambda)$ to the emission coefficient $\epsilon(r, \lambda)$ is given by the Abel transformation:

$$\epsilon(r, \lambda) = -\frac{1}{\pi} \int_r^R \frac{dI(x)}{dx} \frac{1}{\sqrt{x^2 - r^2}} dx. \quad (3.2)$$

There are two major sources of error in this inversion. Due to the differentiation of the measured value, the inversion is sensitive to noise in data. Another error source is that the integrand diverges near $x \sim r$ due to $1/\sqrt{x^2 - r^2}$. To overcome these problems, there have been many inversion methods developed.[15] In this study, the method of Fleurier and Champelle[19] was adopted. Gram's polynomial is used to smooth the experimental data. Near the boundary point ($x \sim r$), dI/dx is interpolated by a second-order polynomial. Equation (3.2) is then integrated analytically. If dI/dx is interpolated by

$$\frac{dI}{dx} = ax^2 + bx + c, \quad (3.3)$$

eq. (3.2) becomes

$$\begin{aligned} \epsilon(r, \lambda) &= -\frac{1}{\pi} \int_{\text{boundary}} \frac{ax^2 + bx + c}{\sqrt{x^2 - r^2}} dx \\ &= -\frac{1}{\pi} \left[\sqrt{x^2 - r^2} \left(\frac{1}{2} ax + b \right) \right. \\ &\quad \left. + \left(\frac{1}{2} ar^2 + c \right) \log[x + \sqrt{x^2 - r^2}] \right]_{\text{boundary}}. \end{aligned} \quad (3.4)$$

Equation (3.4) was used for the integration near $x \sim r$. For other points, the integration was evaluated using Simpson's method.

3.2 Emission profile measurement

Figure 7(a) shows the intensity distribution of the CV $1s^2$–$1s3p$ line along the direction perpendicular to the dispersion direction. This spectrum was obtained about 100 μm away from the target surface along the z direction. For this measurement, the data was obtained with a 10 ns time window gating, 50 ns after the plasma was generated.

As discussed in §2, the spectrometer has a spatial resolution of about 18 μm. In this work, we have selected the data points [solid dots in Fig. 7(a)] separated by 200 μm on the image position. This implies that these data points represent a separation of about 100 μm in the source position, which is larger than the spatial resolution. This ensures that data points are not contaminated. As shown in Fig. 7(a), the dot points were interpolated by a spline method, and were then used in the Abel inversion process.

The intensity distribution is slightly asymmetric and the difference is less than 20%. The difference is large near the optical axis. This may come from experimental error and the asymmetry of the high-intensity-emission area. In this work, both sides are averaged and the deviation from the average is indicated as an error bar.

Figures 7(b) and 7(c) show the result of the inversion, the emission profile. For the CV $1s^2$–$1s3p$ line in Fig. 7(b), about 50% of the total emitted energy is concentrated within a re-

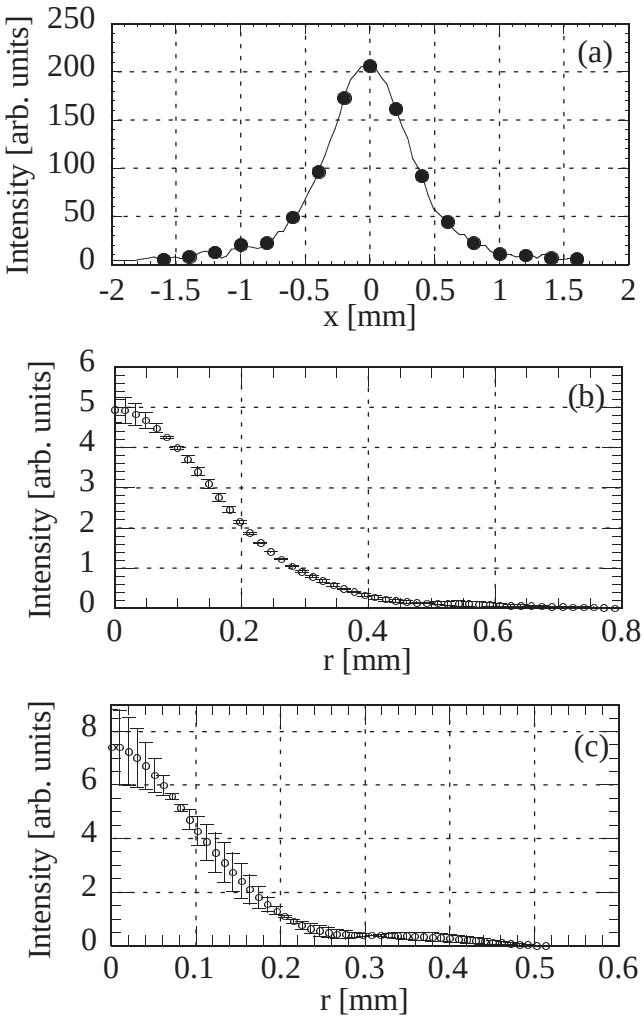

Fig. 7. (a) Measured intensity distributions in the x' direction in Fig. 1 (b) of the CV $1s^2$–$1s3p$ line. Dot points are separated by 200 μm. Emission profile of (b) the CV line and (c) the CVI line, obtained through the Abel inversion. The error bar is mainly due to the asymmetry of the measured data.

gion of 110 μm radius. Figure 7(c) shows the emission profile of the CVI L_β line. For this line, the degree of asymmetry is larger than that of the previous one. This may come from the fact that the line intensity was weaker than the CV $1s^2$–$1s3p$ line so that the experimental error is much larger than in the previous line. In this case the 50% of the total emitted line intensity is concentrated within a region of approximately 76 μm radius. The emission region of the CV ion is more spatially extended than that of the CVI ion.

4. Conclusion

The spatial imaging property of a flat-field spectrometer was studied by ray-tracing and agreed well with experimental measurements using laser-produced carbon plasmas.

When the spectrometer is stigmatic at a 10 nm wavelength, ray-tracing simulation shows that a source displaced by about ± 1 mm along the x direction, ± 15 mm along the y direction, and ± 50 μm along the z direction in the source position, as in Fig. 1, can be imaged with a spatial resolution of about 18 μm, which is in good agreement with the experimental measurement results.

This result was applied to the experimental data obtained from laser-produced carbon plasma spectra to measure emission profiles as a function of the radial distance from the optical axis. Assuming cylindrical symmetry, the Abel inversion was used. For laser-produced carbon plasmas, the CV $1s^2$–$1s3p$ line was distributed within a region of about 110 μm radius, and the CVI L_β line within a region of about 76 μm radius. This indicates that the emission area of the CV ion is more spatially extended than that of the CVI ion.

Acknowledgements

This work has been supported in part by the Basic Science Research Inst., Department of Education (Grant No. BSRI-98-2439), the interdisciplinary research program of KOSEF (Grant No. 1999-1-111-001-5), and the Brain Korea 21 project.

1) M. Galanti and N. J. Peacock: J. Phys. B **8** (1975) 2427.
2) H. J. Shin, D. E. Kim and T. N. Lee: Phys. Rev. E **50** (1994) 1376.
3) E. Jannitti, P. Nicolosi and G. Tondello: Physica C **124** (1984) 139.
4) J. A. R. Samson: *Techniques of Vacuum Ultraviolet Spectroscopy* (Wiley, New York, 1967).
5) G. Tondello: Opt. Acta **26** (1979) 357.
6) H. S., D. E. Kim and T. N. Lee: Rev. Sci. Instrum. **66** (1995) 4222.
7) T. Harada and T. Kita: Appl. Opt. **19** (1980) 3987.
8) T. Kita, T. Harada, N. Nakano and H. Kuroda: Appl. Opt. **22** (1983) 512.
9) N. Nakano, H. Kuroda, T. Kita and T. Harada: Appl. Opt. **23** (1984) 2386.
10) W. Schwanda, K. Eidmann and M. C. Richardson: J. X-ray Sci. Tech. **4** (1993) 8.
11) I. W. Choi: Ph. D. Thesis, Department of Physics, Korea Advanced Institute of Science and Technology, Taejon, Republic of Korea 1996.
12) P. Fan, Z. Zhang, J. Zhou, R. Jin and Z. Xu: Appl. Opt. **31** (1992) 6720.
13) I. H. Hutchinson: *Principles of Plasma Diagnostics* (Cambridge University Press, Cambridge, 1987).
14) H. R. Griem: *Princiles of Plasma Spectroscopy* (Cambridge University Press, Cambridge, 1997) Cambridge Monographs on Plasma Physics.
15) M. J. Buie, J. T. P. Pender, J. P. Holloway, T. Vincent, P. L. G. Ventzek and M. L. Brake: J. Quant. Spectrosc. Radiat. Transfer **55** (1996) 231.
16) B. Lai and F. Cerrina: Nucl. Instrum. Methods A **266** (1988) 544.
17) M. C. Marconi, J. J. Rocca and G. J. Krausse: J. Phys. E **22** (1989) 849.
18) S. Aoki, T. Ogata, S. Sudo and T. Onuki: Jpn. J. Appl. Phys. **31** (1992) 3477.
19) C. Fleurier and J. Champelle: Comput. Phys. Commun. **7** (1974) 200.